Α

y



# Simulation of Vacuum Chamber Pressure Distributions with Uncertainty Quantification

Charles P. Lipscomb\* and Iain D. Boyd† *University of Colorado Boulder, Boulder, Colorado 80305*Kaelan B. Hansson‡

AMA, Inc., NASA Ames Research Center, Mountain View, California 94035 and

Joshua D. Eckels<sup>§</sup> and Alex A. Gorodetsky<sup>¶</sup> *University of Michigan, Ann Arbor, Michigan 48109* 

https://doi.org/10.2514/1.B39954

One of the primary challenges in understanding variations in electric propulsion performance between ground tests and space operations lies in the pressure distribution within the test vacuum chamber. The chamber backpressure is much higher than experienced in space, modifying thruster performance and plume dynamics. Numerical simulation is a key element in determining the background conditions in nonideal vacuum chamber environments. An important parameter for the accurate simulation of chamber backpressure is the sticking coefficient, which sets the probability that an atom will stick to a cryogenic panel used to pump away the plume gases. This quantity can be used to model vacuum pumps in particle-based kinetic numerical methods. In this work, a three-dimensional direct simulation Monte Carlo code is used to model neutral xenon atoms flowing from the anode of the H9 Hall effect thruster within a large vacuum test facility. Simulated pressures are compared with ion gauge pressure measurements to infer the effective sticking coefficient of the chamber's vacuum pumps. A pressure-predicting surrogate model is developed for inference of pump sticking coefficients and for uncertainty quantification. This information facilitates accurate and useful kinetic simulations of electric propulsion thruster plasma plumes in vacuum chambers.

### Nomenclature

pump area, m<sup>2</sup>

collision diameter, m

experimental data

$\boldsymbol{F}$	=	force, N
f	=	pumping speed, m <sup>3</sup> /s
g	=	relative speed, m/s
Kn	=	Knudsen number
$k_B$	=	Boltzmann constant, J/K
$L_C$	=	characteristic length of the system, m
m	=	mass, kg
$\dot{m}$	=	mass flow rate, kg/s
$\mathcal{N}$	=	normal distribution
$N_{\rm pairs}$	=	total particle pairs to be assessed for collision
$N_P$	=	number of macroparticles
n	=	number density, m <sup>-3</sup>
ref	=	reference value
$S_T$	=	total-order Sobol' index
$S_1$	=	first-order Sobol' index
T	=	gas temperature, K
$T_p$	=	pump temperature, K
Ú	=	uniform distribution

Presented as Paper 2024-2369 at the AIAA SciTech Forum, Orlando, FL, January 8–12, 2024; received 23 December 2024; accepted for publication 25 August 2025; published online 10 October 2025. Copyright © 2025 by the American Institute of Aeronautics and Astronautics, Inc. All rights reserved. All requests for copying and permission to reprint should be submitted to CCC at www.copyright.com; employ the eISSN 1533-3876 to initiate your request. See also AIAA Rights and Permissions https://aiaa.org/publications/publish-with-aiaa/rights-and-permissions/.

\*Ph.D. Candidate, Ann and H. J. Smead Department of Aerospace Engineering Sciences; charles.lipscomb@colorado.edu.

<sup>†</sup>H. T. Sears Memorial Professor, Ann and H. J. Smead Department of Aerospace Engineering Sciences; iain.boyd@colorado.edu. Fellow AIAA.

<sup>‡</sup>Research Scientist, Aerothermodynamics Branch.

§Ph.D. Candidate, Department of Aerospace Engineering. Student Member AIAA.

Assistant Professor, Department of Aerospace Engineering, Member AIAA.

 $\alpha$  = accommodation coefficient  $\Delta t$  = simulation time step, s  $\theta_{cp}$  = cryopump sticking coefficient  $\theta_{cs}$  = cryosail sticking coefficient  $\lambda$  = mean free path, m  $\nu$  = collision frequency s<sup>-1</sup>  $\nu$  = particle velocity, m/s  $\sigma$  = collisional cross section, m<sup>2</sup>

## I. Introduction

E LECTRIC propulsion thrusters have become widely used for station-keeping and orbit-raising due to their high specific impulse, longevity, and reliability [1]. Hall effect thrusters (HETs) are particularly attractive due to the relative simplicity of their design and their high thrust-to-power ratios [2]. The higher specific impulse of electric propulsion over chemical propulsion allows mission designers to allocate less mass for onboard propellant, reducing launch costs and/or increasing the payload mass allowance. High-power electric propulsion (~100 kW) offers the potential for rapid and fuel-efficient space travel. For the development and deployment of high-power electric propulsion, thrusters must be tested in vacuum chambers on Earth, as testing in space is prohibitively expensive. Increasing the power of an electric propulsion system tested in a vacuum chamber leads to a higher mass flow rate of the thruster, which reduces the vacuum chamber's ability to replicate the space environment [3,4]. Due to limitations in facility pumping capacity imposed by chamber surface area constraints, a higher mass flow rate results in increased facility backpressure. Elevated background pressures alter the amount of gas ingested by the thruster, the production of charge-exchange ions, and the divergence of the plume.

To reliably extrapolate thruster performance and lifespan for inspace operations, it is essential to complement ground-based tests with predictive models. Because vacuum chambers cannot fully replicate the space environment, these models serve as a bridge, translating chamber data into reliable predictions of in-space behavior. A computational model that accurately reproduces vacuum chamber measurements is more likely to yield realistic predictions of thruster

performance and lifetime in space environments. Achieving this accuracy requires incorporating physics unique to the vacuum chamber environment, particularly those associated with the chamber's vacuum pumps.

An accurate model of facility vacuum pumps is required to calculate the spatial variations in chamber backpressure. Operating at extremely cold temperatures, cryogenic vacuum pumps remove gas by freezing it onto their surfaces. This process can be effectively modeled by assigning sticking coefficients to the pump surfaces. The sticking coefficient sets the fraction of particle-pump interactions that result in sticking versus reflection. This work adopts an approach for inferring pump sticking coefficients by comparing simulated pressure distributions with pressure measurements [5]. Since the employed gas dynamics model relies on uncertain inputs, the output of the model is also uncertain. Uncertainty quantification (UQ) applied to quantities like chamber backpressure is essential for confidently extrapolating thruster performance and lifetime from vacuum chambers to space environments. The remainder of this paper presents the experimental setup in Sec. II, the numerical methods in Sec. III, the results in Sec. IV, and the conclusions in Sec. V.

## II. Experimental Overview

This section details the experimental setup of the vacuum facility, the ionization gauges used for pressure measurements, and the configurations of the Hall thruster. Experiments involve flowing neutral gas into the vacuum chamber and making steady-state pressure measurements. The data from these experiments is used to infer the characteristics of the facility's vacuum pumps.

#### A. Vacuum Facility

All experiments are performed in a cylindrical chamber that is 9 m long and 6 m in diameter. The chamber is equipped with two types of vacuum pumps. The first type of pump, referred to as a cryopump, is the PHPK-TM1200i re-entrant vacuum pump. The chamber is populated by 13 cryopumps, each of which is housed in a baffled, liquid-nitrogen-cooled casing. The second type of pump, referred to as cryosails, is a liquid-nitrogen-free cryogenic pump [6]. At the time of these experiments, there were a total of five cryosails within the vacuum facility. Figure 1 shows a picture of the interior of

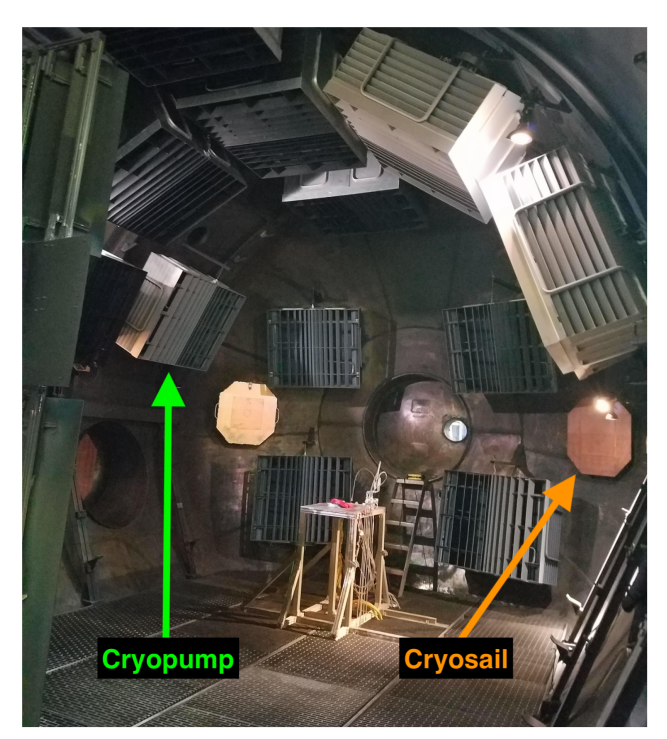


Fig. 1 The interior of the chamber featuring octagonal cryosails and baffled PHPK-TM1200i cryopumps.

the chamber. The baffled structures in Fig. 1 are the cryopumps, and the octagonal surfaces are the cryosails.

Two sets of experimental pressure measurements are collected in this work. One set comes from experiments using a high-pressure pump configuration, and the other set uses a low-pressure pump configuration. The high-pressure configuration has three cryopumps active along the top of the chamber as well as two inactive pumps with active liquid nitrogen shrouds. The low-pressure configuration uses 13 cryopumps and four cryosails. Figure 2 shows a rendering of each configuration as well as an illustration of the computational domain used in this work. As shown in Fig. 2, the cryopumps are mounted along the interior sidewalls and ceiling of the chamber. These cryopumps are arranged symmetrically within the chamber: four are mounted on the rear end-cap; three form a transverse row extending from one sidewall, across the ceiling, to the opposite sidewall in a plane aligned with the thruster; five are arranged similarly in a second transverse row approximately 1.5 m downstream of the thruster; and one additional cryopump is mounted on the ceiling approximately 3 m downstream of the thruster. The four employed cryosails are also mounted symmetrically within the chamber. Two are positioned between the cryopumps on the chamber's end-cap, while the other two are mounted on the sidewalls in the thruster's exit plane, approximately 1 m below the thruster centerline. The thruster is mounted with its center located approximately 2.5 m above the chamber floor and 3 m forward of the rear end-cap, oriented to face the beam trap.

### **B.** Ionization Gauges

Two Granville-Phillips 370 hot-cathode Bayard-Alpert Stabil-ion gauges running on a 370 series vacuum gauge controller are used for measuring chamber pressure. These gauges are capable of measuring pressures in the range of  $10^{-10}$  to  $10^3$  Torr. One ionization gauge, referred to as gauge 1, faces downstream (the direction in which the thruster expels gas) and is located 1 m away from the thruster in the thruster exit plane (as is recommended in [7]). The other ionization gauge, referred to as gauge 2, faces away from the thruster and is located 1 m behind the thruster (the front of the thruster being defined as the side with the acceleration channel, which points toward the beam trap). Figure 3 shows the approximate locations of the ionization gauges in the chamber. Pressure measurements from both gauges were originally calibrated for nitrogen by the manufacturer and corrected to xenon using a spinning rotor gauge. Although the gauge calibration expired in July 2023, all pressure measurements used in this study were acquired in May 2022, before the expiration date. The accuracy of the gauges is taken to be  $\pm 10\%$  based on heritage data. This estimate does not account for thermal effects that may influence gauge behavior in vacuum environments. As discussed in Ref. [7], ion gauge readings are sensitive to both the local gas temperature and the gauge temperature. For the room-temperature gas conditions present in this study, temperature effects from the gas are expected to be negligible. The gauge temperature can deviate from ambient due to the lack of convective cooling and the presence of nearby cryogenic surfaces. These thermal effects are not explicitly corrected for in the ion gauge measurements and are acknowledged as a source of potential uncertainty and an area for future refinement.

### C. Hall Thruster

The thruster used in all experiments is the magnetically shielded 9-kW H9 HET. The centrally mounted lanthanum hexaboride cathode, the anode/gas distributor, and the acceleration chamber geometry of the H9 were all inherited from the unshielded 6-kW H6 HET. More information about the H9 may be found in [8]. In all experiments, neutral xenon atoms flow through the anode of the H9 without a plasma discharge. Mass flow rates and the corresponding pressure measurements from both ionization gauges are reported in Tables 1 and 2 for the high- and low-pressure configurations, respectively.

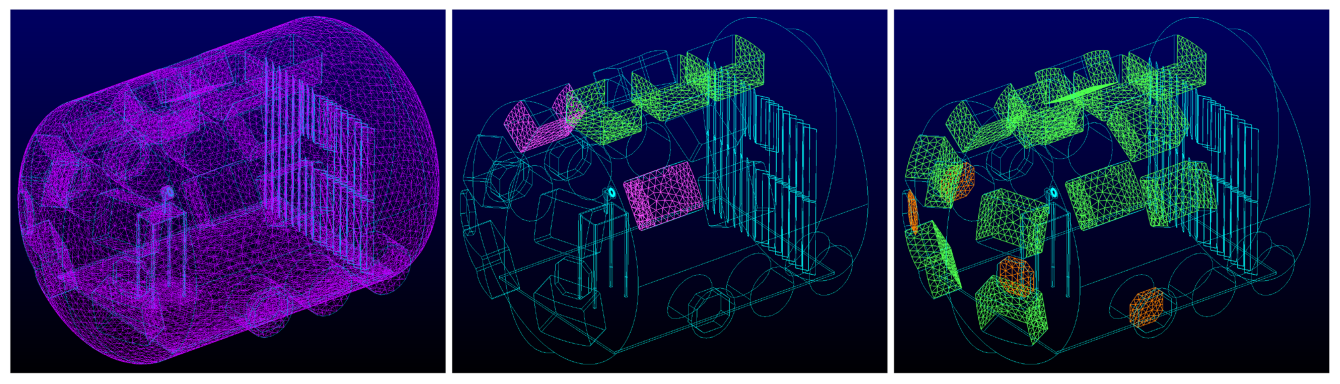


Fig. 2 Computational domain showing vacuum chamber (left), high-pressure (center), and low-pressure (right) configurations with cryopumps (green), cooled inactive pumps (pink), and cryosails (orange).

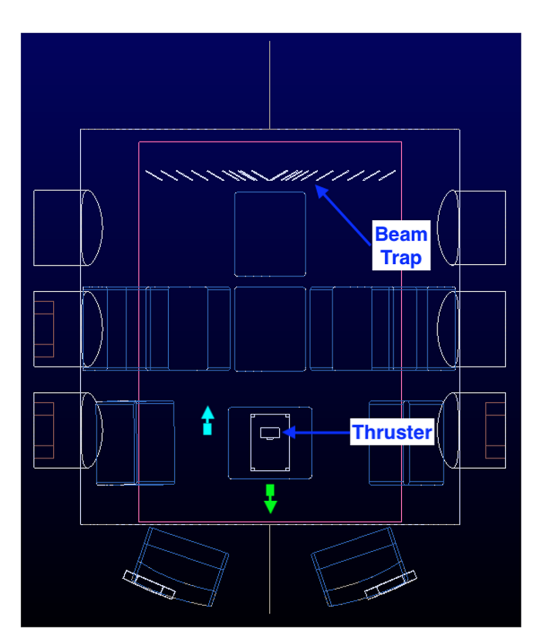


Fig. 3 Top-down view of the facility showing ion gauge locations and orientations (teal and green), along with the thruster and beam trap positions.

Table 1 Experimental pressure measurements for the high-pressure configuration with neutral xenon flowing through the H9 HET at various mass flow rates

Mass flow rate, sccm	Gauge 1 pressure, $\mu$ Torr	Gauge 2 pressure, μTorr
100	11.6	10.6
200	19.9	18.9
300	25.9	26.5
400	31.6	33.9

Table 2 Experimental pressure measurements for the low-pressure configuration with neutral xenon flowing through the H9 HET at various mass flow rates

Mass flow rate, sccm	Gauge 1 pressure, μTorr	Gauge 2 pressure, μTorr
250	5.2	4.0
300	6.1	4.6
350	6.9	5.3
400	7.6	6.0

#### III. Numerical Methods

## A. Physics-Based Modeling

The modeling approach for simulating dilute gas flow ejected from the thruster within the vacuum chamber involves using a direct simulation Monte Carlo (DSMC) code. The code, known as MONACO, is a parallelized 3D DSMC code that accommodates unstructured meshes. MONACO uses static boundary conditions and provides time-averaged steady-state results. Kinetic descriptions of gases, the DSMC method, and the boundary conditions used in this work are discussed in the following three subsections.

### 1. Kinetic Modeling of Gas Dynamics

The extent of rarefaction of a gas flow may be quantified by the following nondimensional parameter known as the Knudsen number:

$$Kn = \frac{\lambda}{L_C} \tag{1}$$

where  $\lambda$  is the mean free path of the gas and  $L_C$  is a characteristic length of the system. When Kn < 0.01, the continuum assumption is valid and fluid conservation equations accurately describe the system. The case when Kn > 1 is known as free molecular flow. In this regime, a kinetic description of the flow is needed. A kinetic description is necessary for large-Knudsen-number, nonequilibrium flows in which the lack of collisions permits non-Maxwellian velocity distribution functions. The transitional regime, where typical electric propulsion plumes reside [9], is characterized by 0.01 < Kn < 1. In this regime, collisions are important but insufficient for bringing the system into equilibrium. When modeling transitional gases, it is necessary to use a kinetic approach.

To accurately resolve the distribution functions within a rarefied gas, kinetic methods that capture the physics of the Boltzmann equation are required [10]. This work employs a particle-based kinetic approach in which the motion of individual macroparticles that represent a much larger number of real particles is tracked through the computational domain. The transport of neutrals and the collision dynamics thereof are simulated using the DSMC method [11].

## 2. Direct Simulation Monte Carlo

The DSMC method leverages key physical properties of dilute gases to efficiently and accurately model flow behavior [10]. One such property is that molecules primarily move in free flight without interacting for durations comparable to the local mean collision time, enabling the separation of particle translation from particle–particle collisions. This separation simplifies modeling and reduces computational cost by eliminating the need for continuous collision tracking. When collisions occur, the impact parameters and initial orientations of molecules are random, reflecting the stochastic nature of molecular interactions. This randomness lowers computational expense compared to deterministic approaches, such as those

used in molecular dynamics. Additionally, although the number of actual molecules within each cubic mean free path is immense, simulating only a small fraction of model particles is sufficient to capture the essential characteristics of the flow. This statistically justified assumption allows DSMC to produce highly accurate distribution functions while maintaining computational feasibility.

To further decrease simulation run time, MONACO is highly parallelized, allowing it to be run in a distributed sense across many CPUs on a supercomputer. MONACO is equipped to simulate flows on unstructured computational grids, enabling the simulation of gas flows within complicated geometries. Collisions in the DSMC method are performed stochastically. The No-Time-Counter scheme [11] is used to calculate the total number of potential collision pairs within each computational cell:

$$N_{\text{pairs}} = \frac{1}{2} N_P n(\sigma g)_{\text{max}} \Delta t \tag{2}$$

where  $N_p$  is the total number of macroparticles, n is the number density,  $(\sigma g)_{\max}$  is an estimate of the maximum value of the product of the collisional cross section with the relative speed of the colliding particles, and  $\Delta t$  is the time step. Whether or not a given pair collides is decided by comparing the collision probability with a random number. The collision probability is calculated as the ratio of  $\sigma g$  to  $(\sigma g)_{\max}$ . Various collision models yield different values of  $\sigma$ . MONACO utilizes the variable hard-sphere model [12] to obtain momentum exchange collision cross sections. In this model, the cross section is a function of relative speed:

$$\sigma = \sigma_{\text{ref}} \left( \frac{g_{\text{ref}}}{g} \right)^{-2\omega} \tag{3}$$

where g is the relative speed, and the power law exponent  $\omega$  is a fitting parameter related to the gas viscosity.

The DSMC model calculates pressure using the ideal gas law:

$$p = nk_BT \tag{4}$$

where  $k_B$  is Boltzmann's constant and T is the temperature of the gas. The temperature is computed as the average of the translational temperatures in the three coordinate directions:

$$T = \frac{1}{3}(T_x + T_y + T_z) \tag{5}$$

Each directional temperature is computed as follows:

$$T_x = \frac{m}{k_B} \left( \frac{\sum C_x^2}{\sum N_p} - \langle C_x \rangle^2 \right)$$
 (6)

$$T_{y} = \frac{m}{k_{B}} \left( \frac{\sum C_{y}^{2}}{\sum N_{p}} - \langle C_{y} \rangle^{2} \right) \tag{7}$$

$$T_z = \frac{m}{k_B} \left( \frac{\sum C_z^2}{\sum N_p} - \langle C_z \rangle^2 \right)$$
 (8)

where m is the particle mass,  $C_i$  represents the peculiar velocity component in the ith direction, and  $N_p$  is the number of particles in the cell. This means of calculating pressure assumes that the velocity distribution is close enough to Maxwellian that the translational kinetic energy can be meaningfully represented by a scalar temperature. Even though the pressure is being queried in low-density regions of the plume where collisions are infrequent, the gas is likely in thermal equilibrium due to interactions with the chamber walls.

#### 3. Boundary Conditions

The number density, velocity, and temperature of xenon atoms are prescribed over an annulus representing the thruster exit. The atom velocity distribution is modeled as a Maxwellian, characterized by a

bulk velocity equal to the local speed of sound and a temperature of 300 K. The sonic assumption at the thruster exit is based on 1D gas dynamics, where a subsonic flow will accelerate to sonic conditions at a channel exit [13]. The number density is obtained from the following mass flow rate equation:

$$\dot{m} = Amnv \tag{9}$$

where  $\dot{m}$  is the mass flow rate, m is the propellant molecular mass, A is the area of the thruster exit plane, n is the number density, and v is the velocity. Particle-surface interactions are modeled with an accommodation coefficient that sets the probability that a particle interacting with a solid wall will reflect diffusely rather than specularly. An accommodation coefficient of 0.9 means that 90% of particle reflections will be diffuse and 10% will be specular. Walls are set to 300 K in the simulations. The vacuum pumps are modeled using a sticking coefficient that sets the fraction of pump interactions that result in removal of an incident atom. Each pump of a given type is assumed to have the same sticking coefficient and the same surface temperature. This assumption simplifies the model and enables tractable inference. Quantifying the effect of this simplification is left to future work. The cryopump sticking coefficient inferred in this work represents an effective sticking coefficient for particles that interact with the chevroned orifice of the cryopump. This effective coefficient is expected to be significantly lower than values measured for the helium-cooled inner cryo-surface, as many particles are not transmitted through the chevrons. Cryopumps are nominally set to 85 K, and cryosails are set to 40 K.

#### B. Uncertainty Quantification

This section summarizes sources of uncertainty in the DSMC model, the Bayesian inference approach used for model calibration, and the methods applied for forward uncertainty quantification.

## 1. Sources of Uncertainty

Uncertainty arises in the DSMC evaluation of vacuum chamber pressure due to imprecise knowledge of the experimental conditions, the model fit coefficients, and natural variability in the system (i.e., measurement uncertainty, numerical tolerance, etc.). Uncertainty in the model inputs confounds understanding of the model outputs, and so this work seeks to quantify output uncertainty by propagating input uncertainty through the DSMC code. Input uncertainty is represented by assigning a probability distribution function (PDF) to each input that encodes a prior belief in their value and degree of variability (i.e., wider distributions encode a greater degree of uncertainty in the value of the inputs). Note that uncertainty may also arise from the specific form of the physical DSMC model itself (from physical assumptions, numerical approximations, etc.), but the scope of this study is focused on quantifying only input uncertainty.

Table 3 summarizes the model input uncertainties for the DSMC pressure predictions. Since only an expected range of values is known for each input, an uninformative uniform prior distribution between upper and lower bounds is assigned (note that given enough data, the calibration results are insensitive to the specific

Table 3 Summary of input uncertainty for the DSMC pressure model

pressure model						
Parameter	Symbol	Unit	Distribution	Domain		
Collision diameter	d	nm	U(0.564, 0.584)	[0.564, 0.584]		
Mass flow rate	$\dot{m}$	sccm	$\mathcal{U}(\pm 1\%)$	[100, 400]		
Wall accommodation coefficient	α		U(0.9, 1)	[0.9, 1]		
Cryopump surface temperature	$T_p$	K	<i>U</i> (75,95)	[75, 95]		
Cryopump sticking coefficient	$\theta_{cp}$		U(0.2, 0.6)	[0.2, 0.6]		
Cryosail sticking coefficient	$\theta_{cs}$		U(0.2, 1)	[0.2, 1]		

choice of prior here). The uncertainty in the collision diameter comes from low-temperature, low-pressure xenon viscosity data [14]. The mass flow rate is controlled by a mass flow controller (ALICAT MC-500SCCM-D) with  $\pm 1\%$  accuracy and  $\pm (0.1\%$  of reading + 0.02% of full scale) repeatability. The wall accommodation coefficient uncertainty is reported in [15]. Appropriate bounds for the pump sticking coefficients are informed by [5]. Cryopump casings are nominally set to 85 K; helium-cooled pumping surfaces inside the cryopump envelope are not explicitly modeled. While the inner, helium-gas-cooled sticking surface operates at about 15 K, it is assumed that returning particles primarily interact with the LN2cooled casing, which is closer to 85 K. A range of 75–95 K is used to represent this surface in the absence of direct measurements. The cryosails are assumed to operate at 40 K. Their surface temperature is measured directly using DT-670 temperature diodes mounted on the exposed sail surfaces, which lack any casing. Because the cryosails contribute significantly less surface area than the cryopumps and their temperatures are measured with an accuracy better than 1 K, uncertainty in their surface temperature is neglected in this analysis. Potential spatial variation across pump surfaces is not modeled, though such variation could influence pumping behavior and is identified as an area for future investigation. The uncertainty in the initial velocity distribution of the gas at the thruster exit is neglected in this study, based on the assumption that collisions with internal chamber structures sufficiently randomize particle motion. Because the primary driver of simulated pressure is the total mass flow rate rather than the detailed velocity distribution, this simplification is considered appropriate.

The goal of this work is twofold: to infer the value of the pump sticking coefficients from experimental pressure data and to understand the effects of the input uncertainty on the model outputs. These tasks are, respectively, accomplished by performing Bayesian inference and forward UQ. Since both require many forward evaluations of the model (on the order of thousands to millions), it is infeasible to use the full DSMC code directly. Each DSMC run takes approximately 5 h on 72 processors. Instead, a surrogate model is constructed to learn the input-output behavior of the DSMC pressure model. Once constructed during an offline training phase, the surrogate model can then be used in place of the full DSMC model for UQ at comparatively negligible computational cost. In this work, we build two surrogates: one for each of the high- and low-pressure experiments. Since the input space is small and we expect the model response to be smooth, we use a simple linear model for both surrogates with third-order polynomial features to map the inputs in Table 3 to the DSMC pressure predictions at two ion gauge locations in the chamber. The coefficients of the linear models are learned by linear least-squares regression with  $L_2$  regularization. A space-filling design is used to sample the input space, where three evenly spaced values of  $\theta_{cp}$  and  $\theta_{cs}$  are used with all combinations of the upper and lower bounds of  $(d, \alpha, T_p)$ . The four mass flow rates in Table 1 are used for the high-pressure surrogate, and three evenly spaced flow rates over the range (100, 400) are used for the low-pressure surrogate. In total, this space-filling design results in 96 total DSMC simulations for training the high-pressure surrogate and 216 total simulations for the low-pressure surrogate.

#### 2. Bayesian Inference

This work seeks to estimate the value of the pump sticking coefficients  $(\theta_{cp}, \theta_{cs})$  given the two sets of experimental data  $(\mathbf{y_1}, \mathbf{y_2})$ , corresponding to the high- and low-pressure data in Tables 1 and 2, respectively. We use the notation  $\mathbf{y_1} = \{y_{1,i}\}_{i=1}^N$  and  $\mathbf{y_2} = \{y_{2,i}\}_{i=1}^N$  to indicate multiple independent measurements  $y_{1,i}$  and  $y_{2,i}$  from each experiment (specifically N=8 in both Tables 1 and 2). Given the data, we want to obtain the posterior distribution  $p(\theta_{cp}, \theta_{cs}, |\mathbf{y_1}, \mathbf{y_2})$  from Bayes's rule:

$$p(\theta_{cp}, \theta_{cs}|\mathbf{y_1}, \mathbf{y_2}) \propto p(\mathbf{y_1}, \mathbf{y_2}|\theta_{cp}, \theta_{cs}) p(\theta_{cp}) p(\theta_{cs})$$
(10)

where  $p(\theta_{cp})$  and  $p(\theta_{cs})$  are the independent priors of the sticking coefficients as given in Table 3. We group all other model uncertainties

present in Table 3 into the term  $\phi=(d,\dot{m},\alpha,T_p)$  with the associated prior  $p(\phi)$  (note that  $\dot{m}$  actually has four terms corresponding to all of the mass flow rates in either Table 1 or Table 2). Ideally, the data is informative for learning the sticking coefficients, and so the posterior would be much narrower than the prior, indicating that uncertainty in the sticking coefficients has been reduced. To compute the posterior, we model each data point as distributed normally about a forward model prediction:

$$y_{1,i} = f_1(\theta_{cp}, \phi)_i + \xi_1,$$
 where  $\xi_1 \sim \mathcal{N}(0, \psi_1^2)$ , and (11)

$$y_{2,i} = f_2(\theta_{cp}, \theta_{cs}, \phi)_i + \xi_2, \text{ where } \xi_2 \sim \mathcal{N}(0, \psi_2^2)$$
 (12)

In these expressions,  $f_1$  and  $f_2$  are the surrogates trained on DSMC simulations to predict pressure at the ion gauge locations in the chamber for the high- and low-pressure cases, respectively. The i subscript denotes the ith data point  $y_{1,i}$  or  $y_{2,i}$  and the corresponding surrogate predictions  $f_1(\cdot)_i$  or  $f_2(\cdot)_i$ . Note that  $f_1$  does not depend on  $\theta_{cs}$ , since the cryosails were only used in the low-pressure experiment. The Gaussian noise terms  $\xi_1$  and  $\xi_2$  encode the modeling choice that experimental measurements are the result of a forward model prediction and additive experimental noise. We assume a 10% experimental noise for the ion gauge measurements in this work, such that  $2\psi_1 = 0.1y_1$  and  $2\psi_2 = 0.1y_2$ . Due to the form of Eqs. (11) and (12) and since the data points are independent, the conditional likelihoods of each dataset are Gaussian PDFs centered at the model evaluations:

$$p(\mathbf{y_1}|\theta_{cp},\phi) = \prod_{i=1}^{N} \frac{1}{\psi_1 \sqrt{2\pi}} \exp \frac{-(y_{1,i} - f_1(\theta_{cp},\phi)_i)^2}{2\psi_1}$$
(13)

$$p(\mathbf{y_2}|\theta_{cp}, \theta_{cs}, \phi) = \prod_{i=1}^{N} \frac{1}{\psi_2 \sqrt{2\pi}} \exp \frac{-(y_{2,i} - f_2(\theta_{cp}, \theta_{cs}, \phi)_i)^2}{\psi_2}$$
(14)

The marginal likelihood  $p(y_1, y_2 | \theta_{cp}, \theta_{cs})$  can then be obtained by integrating over all other uncertainties present in the  $\phi$  term:

$$p(\mathbf{y}_1, \mathbf{y}_2 | \theta_{cp}, \theta_{cs}) = \int p(\mathbf{y}_1, \mathbf{y}_2 | \theta_{cp}, \theta_{cs}, \phi) p(\phi | \theta_{cp}, \theta_{cs}) \,\mathrm{d}\phi \quad (15)$$

$$= \int p(\mathbf{y_1}|\mathbf{y_2}, \theta_{cp}, \theta_{cs}, \phi) p(\mathbf{y_2}|\theta_{cp}, \theta_{cs}, \phi) p(\phi) \, \mathrm{d}\phi \qquad (16)$$

where we have included that  $\phi$  is independent of the sticking coefficients  $(\theta_{cp}, \theta_{cs})$ . We can further simplify Eq. (16) by including that  $y_1$  is independent of  $\theta_{cs}$  and the low-pressure dataset  $y_2$ :

$$p(\mathbf{y_1}, \mathbf{y_2} | \theta_{cp}, \theta_{cs}) = \int p(\mathbf{y_1} | \theta_{cp}, \phi) p(\mathbf{y_2} | \theta_{cp}, \theta_{cs}, \phi) p(\phi) \, \mathrm{d}\phi$$
(17)

Equation (17) intuitively indicates that the likelihood of both datasets  $(y_1, y_2)$  can be factored into the likelihoods of each individual dataset [Eqs. (13) and (14)]. The integration over  $\phi$  is finally performed by a Monte Carlo estimate with M samples:

$$p(\mathbf{y_1}, \mathbf{y_2} | \theta_{cp}, \theta_{cs}) \approx \frac{1}{M} \sum_{i=1}^{M} p(\mathbf{y_1} | \theta_{cp}, \phi^{(i)}) p(\mathbf{y_2} | \theta_{cp}, \theta_{cs}, \phi^{(i)}),$$
where  $\phi^{(i)} \sim p(\phi)$  (18)

and so the posterior in Eq. (10) can be estimated for any set of sticking coefficients ( $\theta_{cp}$ ,  $\theta_{cs}$ ). In this work, we use a pseudo-marginal Markov chain Monte Carlo (MCMC) routine [16] to sample from the full posterior given the unnormalized estimate in Eq. (10).

#### 3. Forward UO

After inferring the posterior distribution of the sticking coefficients, we then study the impact of the input uncertainties on the pressure predictions using the sampling-based Monte Carlo method. For a given mass flow rate, a set of N input samples are drawn:  $\{\theta_{cp,i},\theta_{cs,i}\}_{i=1}^N\sim p(\theta_{cp},\theta_{cs}|\mathbf{y}_1,\mathbf{y}_2)$  and  $\{\phi_i\}_{i=1}^N\sim p(\phi)$ , and then propagated through the surrogate models to obtain the pressure predictions  $y_{1,i}=f_1(\theta_{cp,i},\phi_i)$  and  $y_{2,i}=f_2(\theta_{cp,i},\theta_{cs,i},\phi_i)$ . Statistics of the output distributions  $p(y_1)$  and  $p(y_2)$  can then be estimated using Monte Carlo estimators, e.g., the mean via  $\bar{y}\approx (1/N)\sum_{i=1}^N y_i$ . In this work, we compute credible intervals to compare the model to experimental data using the 5th and 95th percentiles of surrogate predictions.

This work also employs the global, variance-based Sobol' method for sensitivity analysis to quantify how uncertainty in the output arises from uncertainty in the inputs [17,18]. The Sobol' method decomposes the output variance into unique contributions from individual inputs, as well as contributions from interactions between inputs. The quantities of interest in the Sobol' method are the first-order Sobol' indices:  $S_i = V_i/V(y)$ , where  $V_i$  is the partial variance due to the *i*th input  $x_i$ , and V(y) is the total observed variance in the output. The partial variances are computed by

$$V_i = V_{x_i}(\mathbb{E}_{x_{\sim i}}[y|x_i]) \tag{19}$$

where the inner expectation is taken of the output y for a fixed input  $x_i$  over all possible values of the other inputs  $x_{\sim i}$ . The outer variance is then taken over all possible values of  $x_i$ . This work also considers higher-order and total-order indices using sample-based numerical estimators found in [19,20]. All model evaluations required for estimating the Sobol' indices are computed with the surrogates. The results of this global sensitivity analysis indicate not only the inputs with greater impact on output uncertainty but also the relative magnitude of their importance compared to other inputs.

#### IV. Results

#### A. Vacuum Chamber Simulation

A depiction of the 3D unstructured grid used by MONACO is shown in the left panel of Fig. 2. The mesh is composed of approximately 130,000 cells and contains detailed information regarding the location and size of the thruster, the chamber walls, the vacuum pumps, the beam trap, and the floor. Each DSMC simulation takes approximately 5 h to run on 72 processors. The

DSMC simulations contain between 3 and 4 million particles at steady state. Simulations take about 40,000 iterations to reach steady state with a time step of  $10^{-4}$  s. The mean collision time per particle is on the order of  $10^{-2}$  s. Once simulations reach steady state, samples are taken every time step for 100,000 iterations to obtain meaningful statistical results [21]. The relative statistical uncertainty in DSMC pressure estimates scales as the inverse square root of the number of independent samples. Given our sampling over 100,000 time steps with approximately 25 particles per cell, the relative error in the reported pressure values is estimated to be 0.06%. The mean free path of the gas is on the order of 1 m, and the edges of the computational cells do not exceed 0.3 m.

Representative simulated pressure distributions for cold flow through the H9 HET operating in the vacuum chamber using the high-pressure configuration are presented in Fig. 4. The contour plots in Fig. 4 show the pressure in Torr within a 2D slice of the 3D solution for simulations using different pump sticking coefficients. These plots highlight the spatial variability of chamber pressure and demonstrate that increasing the sticking coefficient effectively lowers the overall chamber pressure.

Figure 5 presents xenon temperature contours from the same simulations as Fig. 4. The temperature distributions are largely consistent across the cases, with most of the gas near 300 K, corresponding to the temperature of the chamber walls. As the sticking coefficient increases, the 300 K contour expands due to the pumps becoming more effective at removing particles, resulting in fewer being reflected back into the chamber at low pump temperatures. Low-temperature regions are observed near the pumps, and a distinct low-temperature zone also forms in front of the thruster due to the collimated neutral flow. This feature becomes more pronounced with higher sticking coefficients, as the reduced background density allows the low-temperature core to extend further before collisions with background gas thermalize the flow. Figure 6 presents the magnitude of the bulk velocity in the same 2D slice. While higher sticking coefficients produce slightly larger regions with elevated bulk velocities, most of the chamber—including the regions where the ion gauges are located—exhibits bulk velocities below 10 m/s. This supports the validity of ion gauge pressure measurements, which assume isotropic flow.

Figure 7 illustrates how the pressure at two gauge locations varies with mass flow rate. The plots compare experimental measurements with simulation results for each gauge location, corresponding to the high-pressure pump configuration. The simulations were conducted with sticking coefficients of 0.2, 0.4, and 0.6. From the plots, the

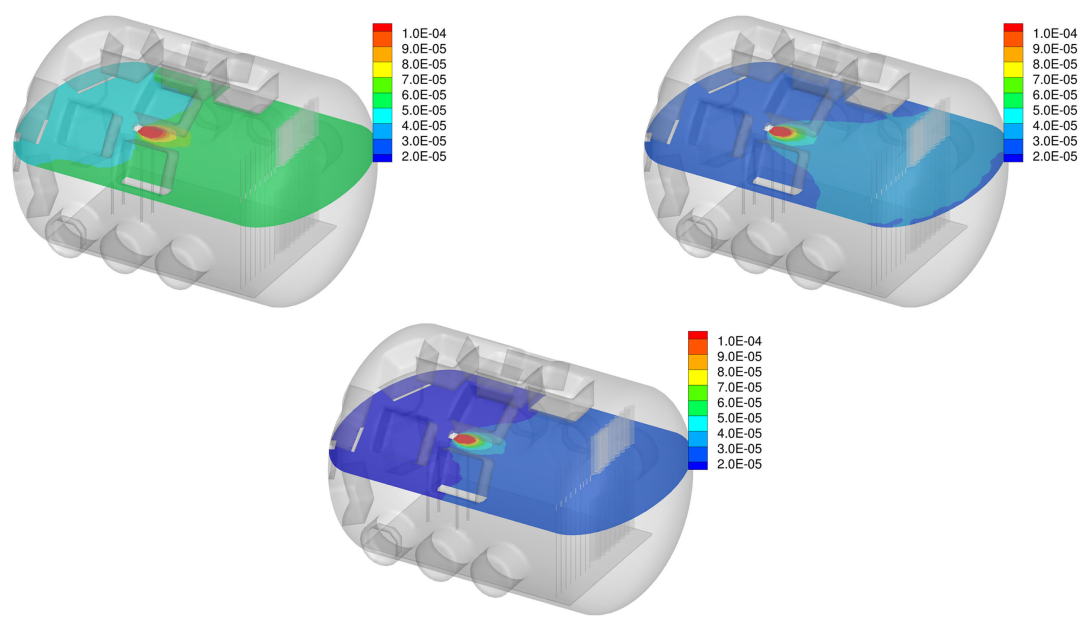


Fig. 4 Pressure (Torr) contours in chamber midplane from cold flow simulations with pump sticking coefficients of 0.2 (upper left), 0.4 (upper right), and 0.6 (bottom).

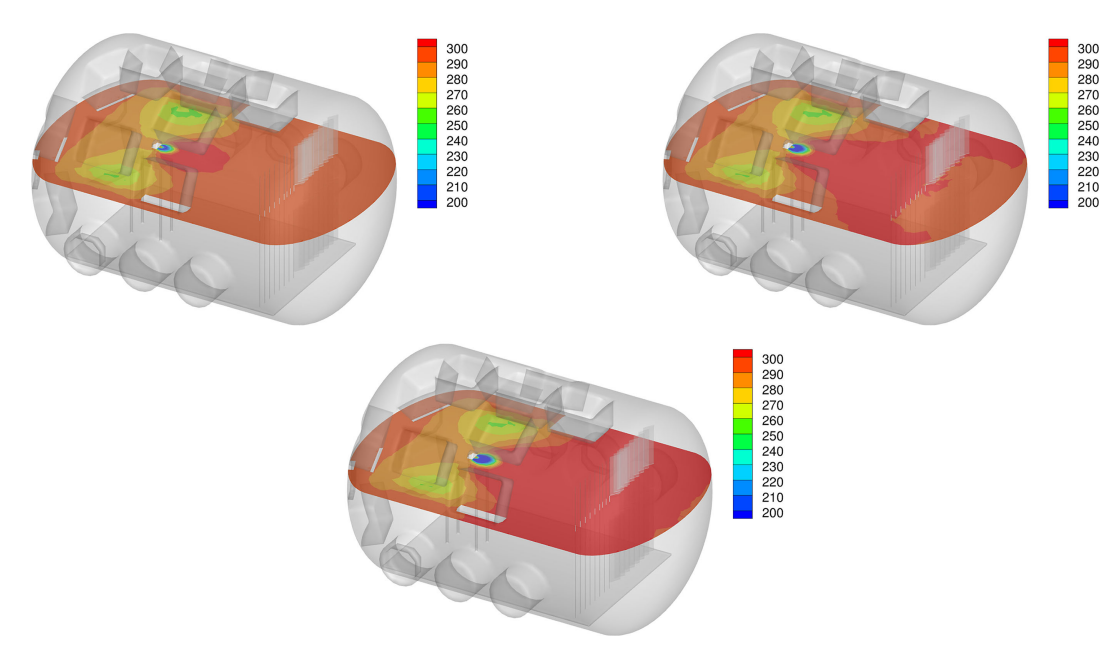


Fig. 5 Temperature (K) contours in chamber midplane from cold flow simulations with pump sticking coefficients of 0.2 (upper left), 0.4 (upper right), and 0.6 (bottom).

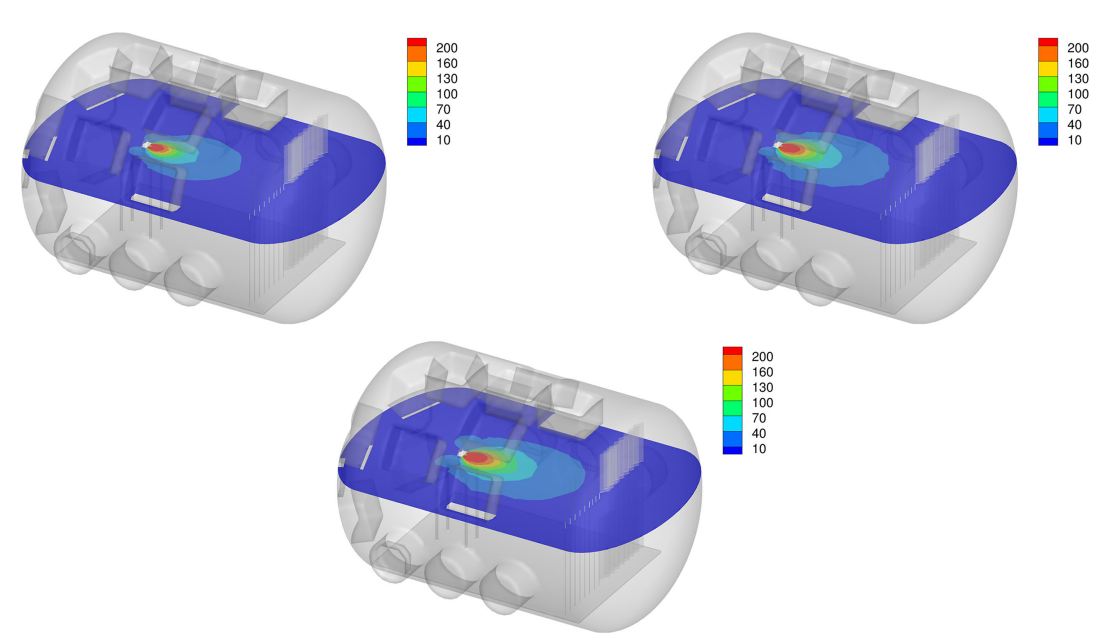


Fig. 6 Bulk velocity magnitude (m/s) contours in chamber midplane from cold flow simulations with pump sticking coefficients of 0.2 (upper left), 0.4 (upper right), and 0.6 (bottom).

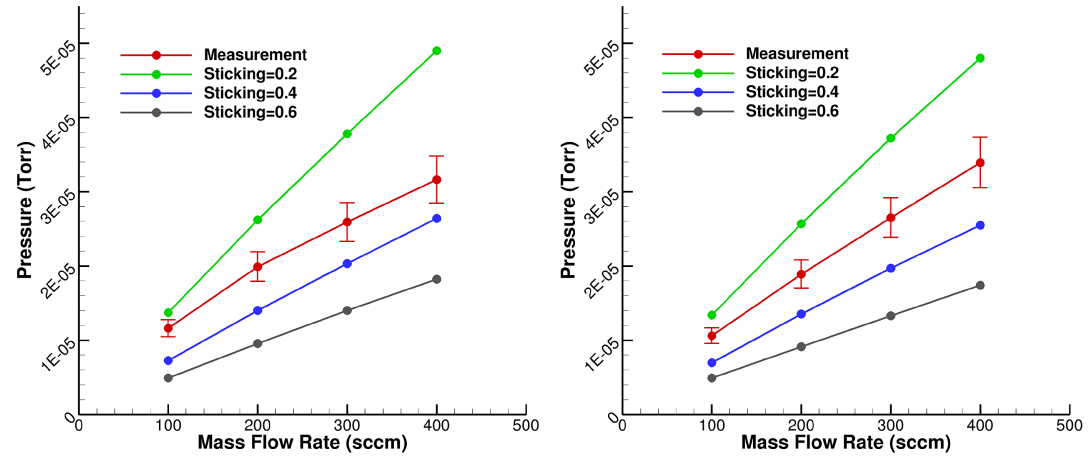


Fig. 7 Pressure vs mass flow rate from simulations and experiments for the high-pressure configuration at gauge 1 (left) and gauge 2 (right). See Fig. 3 for locations.

sticking coefficient of the cryopumps is estimated to lie between 0.2 and 0.4. This initial sweep of sticking coefficients establishes a reasonable range that informs the assigned prior distribution. After refining this prior distribution, a surrogate model was constructed to effectively interpolate and identify the optimal sticking coefficient, accounting for all simulation uncertainties.

## B. Surrogate for the DSMC Model

In order to calibrate the sticking coefficients in the DSMC simulation, two surrogate models were constructed to approximate the DSMC pressure predictions, one for the high-pressure experiment and one for the low-pressure experiment. The DSMC simulations were obtained using a space-filling design over the input space, resulting in 96 total simulations for the high-pressure surrogate and 216 total simulations for the low-pressure surrogate. Each of these datasets was split so that 20% of the data was held out for validating the surrogate's performance. Linear regression was then performed on the remaining 80% of the data to train the coefficients

Table 4  $R^2$  coefficients and relative  $L_2$  errors for high- and low-pressure surrogates on training and validation data ( $R^2$  near 1 and low  $L_2$  indicate good agreement with DSMC)

	Trai	ning	Validation		
Surrogate	$R^2$	$L_2$ , %	$R^2$	$L_2$ , %	
High pressure	>0.99	0.2	>0.99	0.3	
Low pressure	>0.99	0.1	>0.99	0.2	

of the surrogates. The performance of the surrogates on the training and validation sets was evaluated using the  $R^2$  coefficient of determination, as well as the relative  $L_2$  error, defined as

Relative 
$$L_2$$
 Error  $=\frac{\|\mathbf{y} - \hat{\mathbf{y}}\|_2}{\|\mathbf{y}\|_2}$  (20)

where y and  $\hat{y}$  are the vectors of DSMC and surrogate predictions, respectively. Table 4 summarizes the performance of both surrogates, and Figs. 8 and 9, respectively, show the high- and low-pressure surrogate predictions compared to the DSMC simulations.

Both surrogates are shown to have relative errors <0.5% on an independent validation set, indicating good agreement with the DSMC simulation over the input space under consideration. This is again observed in Figs. 8 and 9, where both training and validation set predictions fall along the ideal prediction line, which indicates good agreement between the surrogate and the true model. The goodness of fit forz both surrogates can be attributed to a smooth and simple model response over a small input space, and so the usage of the surrogates in place of the full DSMC simulation for cheap model approximation is justified in the rest of the analysis. Note that while the space-filling design selected training data *a priori*, an adaptive approach may have achieved similar accuracy for a smaller computational cost by more efficiently choosing the training data.

#### C. Calibration of Sticking Coefficients

We now summarize the results of the sticking coefficient calibration procedure described in Sec. III.B.2. MCMC is performed using the surrogate for 20,000 iterations with a burn-in fraction of 10%

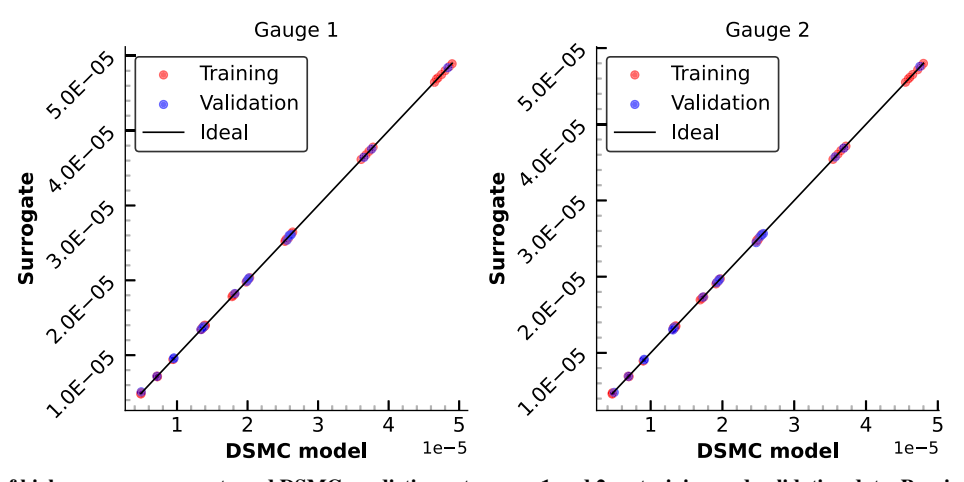


Fig. 8 Comparison of high-pressure surrogate and DSMC predictions at gauges 1 and 2 on training and validation data. Proximity to y = x indicates good agreement.

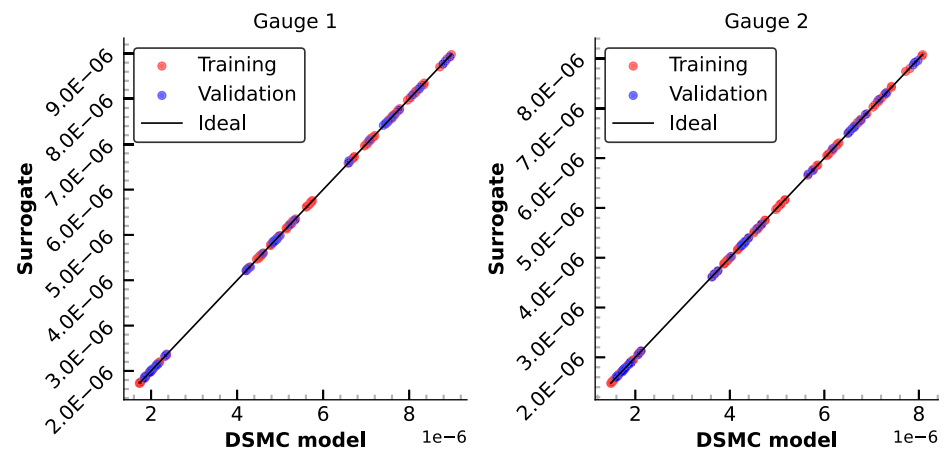


Fig. 9 Comparison of low-pressure surrogate and DSMC predictions at gauges 1 and 2 on training and validation data. Proximity to y = x indicates good agreement.

Table 5 Statistics of 1D marginal posteriors for cryopump  $(\theta_{cp})$  and cryosail  $(\theta_{cs})$  sticking coefficients (modes estimated via Gaussian kernel density maxima)

-			Posterior					
Variable	Prior	Min	5th pctile		95th pctile	Max	Mode	Std dev
$\overline{\theta_{cp}}$	U(0.2, 0.6)	0.241	0.254	0.263	0.272	0.283	0.262	0.006
$\theta_{cs}$	U(0.2, 1)	0.200	0.206	0.266	0.417	0.654	0.221	0.067

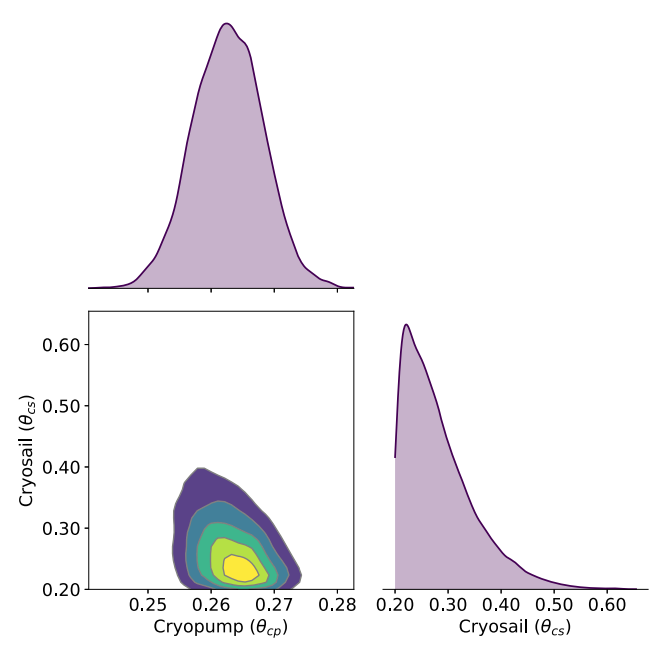


Fig. 10 Joint posterior and 1D marginals for cryopump and cryosail sticking coefficients from 20,000 MCMC samples, smoothed using Gaussian kernel density estimates.

and a resulting acceptance ratio of 72%. The statistics of the posterior marginals for each sticking coefficient are summarized in Table 5 along with the original priors from Table 3 for comparison. Figure 10 additionally shows the joint PDF and 1D marginal distributions of the posterior  $p(\theta_{cp}, \theta_{cs} | \mathbf{y_1}, \mathbf{y_2})$ , smoothed using a Gaussian kernel density estimate. The maximum *a posteriori* (or posterior "mode") is estimated as the maximum of the kernel density estimate for each 1D marginal distribution.

We observe from the statistics in Table 5 and the marginal plots in Fig. 10 that the 1D marginal distribution of the cryopump sticking coefficient is approximately normal about  $\theta_{cp}\approx 0.263$ , which agrees with our prior intuition from the simulations in Fig. 7 and our previous work [22]. Reference [5] reports an inferred sticking coefficient of approximately 0.4 for a similar type of cryopump. Differences between their values and those inferred here likely stem from differences in simulation approaches and fidelity: their simulations used an axisymmetric code, assumed fully diffuse wall reflections, consolidated the total pumping area into a single large pump, and applied a surface temperature of 15 K, representative of the inner cryo-surface rather than the outer casing.

Assuming an isotropic Maxwellian velocity distribution, the sticking coefficient can be estimated from the manufacturer-reported pumping speed using the following expression:

$$\theta = \frac{f}{A\sqrt{\frac{k_BT}{2\pi m}}}\tag{21}$$

where  $\theta$  is the sticking coefficient, f is the pumping speed, and A is the effective pump surface area. For the cryopumps, the reported pumping speed is 35 m<sup>3</sup>/s, and the surface area is 2.7 m<sup>2</sup>. Assuming

xenon gas at 300 K, Eq. (21) gives an estimated sticking coefficient of 0.24. This value is reasonably close to our inferred value of 0.263 and serves as a useful sanity check.

Additionally, we observe a roughly skew-normal distribution of the cryosail sticking coefficient with a most probable value of  $\theta_{cs} \approx 0.221$ , which again agrees with our previous study [22]. The manufacturer-reported pumping speed for the cryosails assumes perfect sticking and therefore does not provide a meaningful basis for estimating the actual sticking coefficient. Since the minimum posterior value of the cryosail sticking coefficient is equal to the prior minimum bound of  $\theta_{cs} = 0.2$ , it is likely that the posterior extends to  $\theta_{cs} < 0.2$ ; this result may warrant extending the training bounds of the surrogate to  $\theta_{cs} < 0.2$  and recalibrating to fully characterize the PDF. However, given the large right-skew in the 1D marginal distribution of  $\theta_{cs}$ , it is likely that we have already captured the majority of the density function.

We finally observe the large reduction in uncertainty from the before posterior as given in Table 5. The reduction in uncertainty was greater for  $\theta_{cp}$  likely because both datasets  $(y_1, y_2)$  were informative for learning the cryopump sticking coefficient (the cryopump was used in both experiments). In contrast, only  $y_2$  is informative for learning the cryosail sticking coefficient, and so the posterior of  $\theta_{cs}$  is much wider. It is likely that additional experiments with the cryosails activated would provide useful data for reducing the uncertainty of  $\theta_{cs}$  further.

### D. UQ and Sensitivity Analysis

Figure 11 compares model predictions to the experimental data in Tables 1 and 2 for the high- and low-pressure experiments, respectively. Predictions for gauge 1 are shown in red, and predictions for gauge 2 are shown in green. The shaded regions indicate the 5th and 95th percentiles of model predictions over N=1000 Monte Carlo samples of the uncertain inputs, i.e.,  $\phi^{(i)} \sim p(\phi)$  and  $\theta^{(i)}_{cp}, \theta^{(i)}_{cs} \sim p(\theta_{cp}, \theta_{cs}|\mathbf{y}_1, \mathbf{y}_2)$  for  $i=1\dots N$ , which induces the uncertain model predictions  $\mathbf{y}_1^{(i)} = f_1(\theta^{(i)}_{cp}, \phi^{(i)})$  and  $\mathbf{y}_2^{(i)} = f_2(\theta^{(i)}_{cp}, \theta^{(i)}_{cs}, \phi^{(i)})$  as notated in Sec. III.B.2. Similar to the MCMC routine, all Monte Carlo model evaluations are computed with the surrogates  $f_1(\cdot)$  and  $f_2(\cdot)$ . The solid lines present the median model predictions.

The increase in model uncertainty for increasing mass flow rates is consistent with the increasing experimental uncertainty (as indicated by the error bars on the experimental data). Overall, the model predictions quantitatively agree well with the experimental data given all uncertainties present in the system. The model predicts the pressure at both gauges well for the high-pressure experiment but underpredicts the pressure at gauge 1 for the low-pressure experiment. One possible explanation is that  $\theta_{cp}$  is primarily tuned to fit the high-pressure data (where  $\theta_{cs}$  is not involved). A lower  $\theta_{cp}$ would have allowed a better fit for the low-pressure data since it would increase the model's pressure predictions at both gauge locations. However, a lower  $\theta_{cp}$  would then result in a less accurate fit to the high-pressure data; the model must trade off accuracy in the high-pressure predictions to additionally fit the low-pressure data. Correspondingly, the calibration procedure reduced  $\theta_{cs}$  to the lowest value allowed under the prior to correct for the under-predicted pressure values in the low-pressure experiment. This negative correlation between  $\theta_{cp}$  and  $\theta_{cs}$  is also apparent in Fig. 10, where higher values of  $\theta_{cp}$  are correlated with lower values of  $\theta_{cs}$  and vice versa. While the model fits well on average, this result does indicate some limitation in using a single set of global sticking coefficients for each pump over all operating conditions.

This work also seeks to quantify the relative impact of each source of uncertainty on the model predictions of pressure. For this, the first-order  $(S_1)$  and total-order  $(S_T)$  Sobol' indices are estimated for the low-pressure case over varying mass flow rates, as shown in Fig. 12 for both the prior and posterior distributions. The indices are estimated with N=10,000 Monte Carlo samples of the uncertain inputs (see Sec. III.B.3 and references therein). The quantity of interest for this sensitivity analysis is the pressure at gauge 1 (the results are very similar when using gauge 2). The first-order indices exist on the domain [0, 1], with higher values indicating a greater

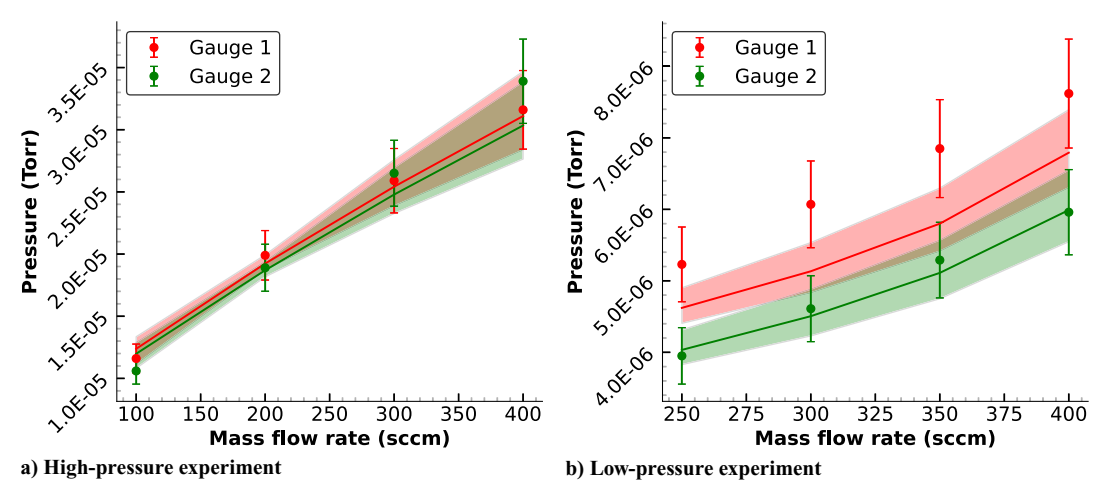


Fig. 11 Calibrated model predictions (lines) vs experimental pressure data (markers) over mass flow rates. Shaded regions show 5th–95th percentiles from 1000 Monte Carlo samples.

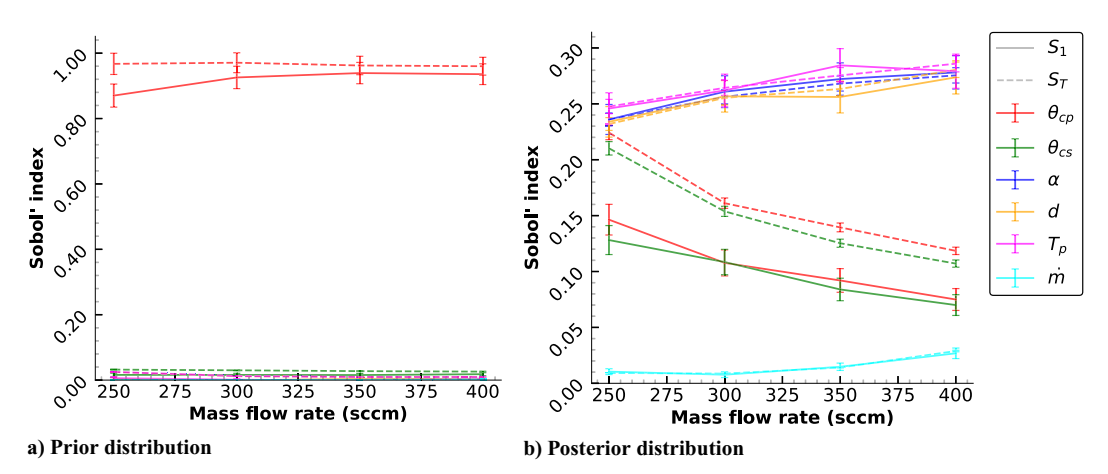


Fig. 12 Sobol'  $S_1$  and  $S_T$  indices for each uncertain input under prior (a) and posterior (b) distributions as functions of mass flow rate with 95% confidence intervals.

contribution of a given input's *unique* contribution to the output uncertainty; the total-order indices additionally account for uncertainty due to interactions between parameters. The fact that  $S_1$  and  $S_T$  are very similar for each parameter indicates that the model is fairly well decoupled, i.e., the model responds mostly to independent changes in each parameter.

Figure 12 clearly demonstrates the intuition that, given the prior distribution, the uncertainty in the cryopump sticking coefficient exerts the most significant influence on model output uncertainty. This is precisely why the current study targets calibration of the sticking coefficients over other parameters. The cryosail sticking coefficient emerges as the second most impactful parameter under the prior distribution, although negligible compared to the cryopump. Notably, the posterior distribution for the sticking coefficients is considerably narrower compared to the prior (see Table 5). This reduction in uncertainty is so pronounced that, in the posterior Sobol' analysis, most other uncertain parameters exhibit a greater relative impact on the output uncertainty than the sticking coefficients. This agrees with the observation that the experimental data was very informative in learning the sticking coefficients.

The 1% uncertainty in the mass flow rate has a negligible effect on the model predictions at low flow rates; however, its impact increases slightly at higher flow rates, as expected. The increasing significance of the collision diameter d at higher flow rates is expected because a greater gas density leads to more frequent collisions. A surprising result is the increasing importance of the wall accommodation coefficient  $\alpha$  and the cryopump surface temperature  $T_p$  for increasing flow rates. This may be attributed to

higher flow rates, leading to increased incident fluxes on the wall and pump surfaces, thereby amplifying the relative influence of  $\alpha$  and  $T_p$ . This interpretation is in agreement with the corresponding increase in total model uncertainty for increasing flow rates shown in Fig. 11. Since the relative sensitivities of the other uncertain input parameters  $(\alpha, d, T_p, \dot{m})$  increase with mass flow rate, a corresponding decrease in relative sensitivity of the sticking coefficients is observed. Lastly, we note that  $S_T > S_1$  for both sticking coefficients under the posterior distribution, which likely indicates some impact of coupling between  $\theta_{cp}$  and  $\theta_{cs}$  on model output uncertainty.

## V. Conclusions

Ground-based electric propulsion testing facilities interfere with thruster performance and plume characteristics. Elevated background pressures caused by the inherently limited pumping capabilities of these facilities alter the amount of gas ingested by the thruster, the production of charge-exchange ions, and the divergence of the plume. These effects and others undermine confidence in the ability of performance and lifetime test results conducted in ground-based facilities to accurately reflect how thrusters will behave in space environments. High-power electric propulsion thrusters will exacerbate these facility effects. Thruster and plume models that account for facility effects must accompany ground-based tests to extrapolate from nonideal chambers to space environments in a predictive fashion. This work is an initial step toward equipping thruster and plume models with a means of accurately recreating the

elevated background pressure experienced by thrusters in ground-based facilities.

Posterior distributions of sticking coefficients have been obtained for the two types of pumps that populate the vacuum chamber. Surrogate models, trained on hundreds of high-fidelity DSMC simulations, enabled detailed Bayesian inference of pump sticking coefficients and thorough uncertainty quantification. The Sobol' method was used for sensitivity analysis and illustrated that calibrating the pump sticking coefficients with pressure measurements reduced their uncertainties effectively, such that they were no longer the most significant contributors to pressure prediction uncertainty under the posterior. Model predictions using the inferred sticking coefficients agree well with experimental ionization gauge measurements within error bounds. The agreement between backpressure measurements and simulation predictions supports the utility of this approach in modeling chamber vacuum pumps. Accurately modeling facility backpressure within simulations of plasma flow experiments is a crucial capability for investigating the role of this facility effect on electric propulsion thrusters and their plumes. Future work will involve the application of these sticking coefficients within simulations of plasma flow experiments of the H9 HET in the chamber to evaluate a coupled thruster-plume model. Another interesting area of future work would be extending the current UQ analysis to optimally design new data collection experiments or simulations to reduce uncertainty further and increase confidence in the model predictions.

## Acknowledgments

This work was supported by NASA through the Joint Advanced Propulsion Institute, a NASA Space Technology Research Institute, under grant number 80NSSC21K1118. Computational resources were provided by the University of Colorado Boulder Research Computing Group, supported by the National Science Foundation, the University of Colorado Boulder, and Colorado State University. Additional resources were provided by the NASA High-End Computing Program through the NASA Advanced Supercomputing Division at Ames Research Center. The authors would also like to thank Professor Ben Jorns and the Plasmadynamic and Electric Propulsion Laboratory at the University of Michigan for conducting the necessary experiments within the Alec D. Gallimore Large Vacuum Test Facility. ChatGPT (OpenAI) was used to assist with copy-editing and phrasing suggestions. All technical content, analysis, and conclusions are the authors' own. Outputs were reviewed and verified.

## References

- [1] Saleh, J. H., Geng, F., Ku, M., and Walker, M. L. R., II, "Electric Propulsion Reliability: Statistical Analysis of On-Orbit Anomalies and Comparative Analysis of Electric Versus Chemical Propulsion Failure Rates," Space Weather—The International Journal of Research and Applications, Vol. 16, No. 10, 2018, pp. 1561–1569. https://doi.org/10.1016/j.actaastro.2017.06.034
- [2] Goebel, D. M., and Katz, I., Fundamentals of Electric Propulsion: Ion and Hall Thrusters, JPL Space Science and Technology Series, Wiley, Hoboken, NJ, 2008, p. 4.
- [3] Hofer, R. R., Peterson, A. Y., and Gallimore, A. D., "Characterizing Vacuum Facility Backpressure Effects on the Performance of a Hall Thruster," 27th International Electric Propulsion Conference, IEPC-01-045, Univ. of Michigan, Ann Arbor, 2001.
- [4] Walker, J. A., Langendorf, S. J., Walker, M. L. R., II, Khayms, V., King, D., and Pertson, P., "Electrical Facility Effects on Hall Current Thrusters: Electron Termination Pathway Manipulation," *Journal of Propulsion and Power*, Vol. 32, No. 6, 2016, pp. 1365–1377. https://doi.org/10.2514/1.B35904

- [5] Walker, M. L. R., II, Gallimore, A. D., Boyd, I. D., and Cai, C., "Vacuum Chamber Pressure Maps of a Hall Thruster Cold-Flow Expansion," *Journal of Propulsion and Power*, Vol. 20, No. 6, 2004, pp. 1127–1131. https://doi.org/10.2514/1.8973
- [6] Viges, E. A., Jorns, B. A., Gallimore, A. D., and Sheehan, J. P., "University of Michigan's Upgraded Large Vacuum Test Facility," 36th International Electric Propulsion Conference, IEPC-2019-653, Univ. of Michigan, Ann Arbor, 2019.
- [7] Dankanich, J. W., Walker, L. R. W., Swiatek, M. W., and Yim, J. T., "Recommended Practice for Pressure Measurement and Calculation of Effective Pumping Speed in Electric Propulsion Testing," *Journal of Propulsion and Power*, Vol. 33, No. 3, 2017, pp. 668–680. https://doi.org/10.2514/1.B35478
- [8] Hofer, R. R., Cusson, S. E., Lobbia, R., and Gallimore, A. D., "The H9 Magnetically Shielded Hall Thruster," 35th International Electric Propulsion Conference, IEPC-2017-232, Univ. of Michigan, Ann Arbor, Jet Propulsion Lab., Pasadena, 2017.
- [9] Choi, M., "Improved Hall Thruster Plume Simulation by Including Magnetic Field Effects," Ph.D. Thesis, Univ. of Michigan, Ann Arbor, 2016.
- [10] Boyd, I. D., and Schwartzentruber, T. E., Nonequilibrium Gas Dynamics and Molecular Simulation, Cambridge Aerospace Series, Cambridge Univ. Press, Cambridge, England, U.K., 2017, pp. 187 and 188.
- [11] Bird, G. A., Molecular Gas Dynamics and the Direct Simulation of Gas Flows, Clarendon Press, Oxford, U.K., 1994.
- [12] Bird, G. A., "Monte-Carlo Simulation in an Engineering Context," Progress in Astronautics and Aeronautics, Vol. 74, 1981, pp. 239–255. https://doi.org/10.2514/5.9781600865480.0239.0255
- [13] Boyd, I. D., Van Gilder, D. B., and Liu, X., "Monte Carlo Simulation of Neutral Xenon Flows in Electric Propulsion Devices," *Journal of Propulsion and Power*, Vol. 14, No. 6, 1998, pp. 1010–1014. https://doi.org/10.2514/2.5366
- [14] Grisnik, S. P., "Measurement of Xenon Viscosity as a Function of Low Temperature and Pressure," 34th Joint Propulsion Conference, AIAA Paper 1998-2503, 1998.
- [15] Agrawal, A., and Prabhu, S. V., "Survey on Measurement of Tangential Momentum Accommodation Coefficient," *Journal of Vacuum Science* and Technology A, Vol. 26, No. 4, 2008, pp. 634–645. https://doi.org/10.1116/1.2943641
- [16] Andrieu, C., and Roberts, G. O., "The Pseudo-Marginal Approach for Efficient Monte Carlo Computations," *Annals of Statistics*, Vol. 37, No. 2, 2009, pp. 697–725. https://doi.org/10.1214/07-AOS574
- [17] Sobol, I. M., "Sensitivity Analysis for Non-Linear Mathematical Models," *Mathematical Modelling and Computational Experiment*, Vol. 1, 1993, pp. 407–414.
- [18] Sobol, I. M., "Global Sensitivity Indices for Nonlinear Mathematical Models and Their Monte Carlo Estimates," *Mathematics and Computers in Simulation*, Vol. 55, Nos. 1–3, 2001, pp. 271–280. https://doi.org/10.1016/S0378-4754(00)00270-6
- [19] Saltelli, A., "Making Best Use of Model Evaluations to Compute Sensitivity Indices," *Computer Physics Communications*, Vol. 145, No. 2, 2002, pp. 280–297. https://doi.org/10.1016/S0010-4655(02)00280-1
- [20] Saltelli, A., Annoni, P., Azzini, I., Campolongo, F., Ratto, M., and Tarantola, S., "Variance Based Sensitivity Analysis of Model Output. Design and Estimator for the Total Sensitivity Index," *Computer Physics Communications*, Vol. 181, No. 2, 2010, pp. 259–270. https://doi.org/10.1016/j.cpc.2009.09.018
- [21] Chen, G., and Boyd, I. D., "Statistical Error Analysis for the Direct Simulation Monte Carlo Technique," *Journal of Computational Physics*, Vol. 33, No. 3, 2017, pp. 668–680. https://doi.org/10.1006/jcph.1996.0148
- [22] Lipscomb, C. P., Boyd, I. D., Hansson, K. B., Eckels, J. D., and Gorodetsky, A. A., "Simulation of Vacuum Chamber Pressure Distribution with Surrogate Modeling and Uncertainty Quantification," AIAA Science and Technology Forum, AIAA Paper 2024-2369, 2024.

J. Rovey Associate Editor